Fracture Simulation of Fiber Reinforced Composite Panels with Holes

Yang Zhang [1], Jialu Guo[1], Zhan Shu[1],Yaojing Guan[1], A.S. Ademiloye[2,*]
[1]*School of Physics，Nanjing University of Science and Technology, Nanjing 210094, China*
[2]*Zienkiewicz Institute for Modelling, Data and AI, Faculty of Science and Engineering, Swansea University, Swansea SA1 8EN, United Kingdom*

Highlights

- Establishing phase-field modeling to investigate the fracture behavior of FRC Panels
- Impact of fiber orientation and hole distribution on FRC fracture behavior
- It was observed that uniform hole distribution improves their mechanical performance
- Under thermal shock, the direction of crack propagation does not strictly follow the fiber angle but tends to grow towards the hole

Abstract

Fiber reinforced composite (FRC) with holes have broad applications in various fields. In this study, the influence of fiber orientation and hole distribution on the fracture behavior of FRC was investigated. A phase-field modeling was established to simulate the fracture process of the composite, and the mechanical performance of unidirectional fiber reinforced composite and woven fiber reinforced composite were analyzed, respectively. Our numerical results showed that fiber orientation and hole distribution have a significant impact on the fracture behavior of FRC. We observed that aligning the fibers parallel to the loading direction led to an increase in the maximum load bearing capacity of the composite. A more uniform hole distribution can enhance the overall mechanical performance of FRC. Furthermore, in the presence of thermal shock, crack propagation tends to grow towards the hole. These findings are of great significance for understanding the fracture behavior of FRC, and for optimizing material design and fabrication processes.

Key Words: Fiber reinforced composite (FRC), Fracture, Phase-field modeling, Fiber orientation, Hole distribution, Thermal shock

---

* Corresponding authors.
E-mail addresses: hfutzy@njust.edu.cn (Yang Zhang); a.s.ademiloye@swansea.ac.uk (A. S. Ademiloye)

1. Introduction

Compared with traditional materials, composite materials have many excellent mechanical properties, such as tunable mechanical performance and high specific strength. Research has shown that the high elastic modulus of fibers plays an important role in enhancing the modulus of composite materials, thereby improving their mechanical properties such as high-temperature deformation resistance and crack resistance [1]. Carbon fiber (CF) reinforced composites [2] have attracted great attention in the aerospace and defense industries due to their outstanding mechanical performance, and have been widely used in engineering fields and even in the biomedical field. Carbon fiber reinforced pyrolytic carbon (PyC) composites not only possess strong mechanical strength and excellent friction performance, but also exhibit outstanding anti-ablation performance, making them suitable for applications in fields such as automotive engineering, aerospace, environmental protection, and biomedicine [3].

Fiber reinforced composite (FRC) with holes have significant applications in various fields due to their lightweight, high strength, high stiffness, and corrosion resistance. In automotive engineering, they can be used for body structures, interior components, and powertrain components to achieve lightweight design and improve fuel efficiency. In the aerospace field, they can be used for structural components, fuel storage and delivery systems, and thermal/acoustic insulation materials to reduce the weight of aircraft and improve performance. Additionally, in the environmental protection field, they can be used as filtering and separating materials, such as air filters and water treatment filters, with excellent filtering performance and efficient resource utilization. With the continuous progress of technology and the increasing demand for material performance, FRC with holes may find more applications in various fields. However, due to the existence of holes, its mechanical property becomes complex. Therefore, it is necessary to investigate the fracture behavior of FRC panels with holes to improve the reliability and safety of modern engineering structures.

Fracture simulation of FRC panels has been the focus of recent research in the field of composite materials. Significant progress has been made through experimental

investigations and numerical simulations. Muhammed et al. [4] proposed a fracture toughness model to predict crack initiation and propagation in unidirectional fiber reinforced composite panels with holes. Huang et al. [5] conducted experimental testing to evaluate the fracture toughness of orthotropic panels with holes. Numerical studies by Dan et al. [6] and Wei et al. [7] focused on simulating crack propagation in panels with holes, considering factors such as hole size, fiber orientation, and loading conditions. Negi et al. [8] developed an anisotropic gradient-enhanced continuum damage model to analyze fracture behavior in layered composite panels with holes. Granados et al. [9] studied composite material fatigue prediction based on series/parallel hybrid theory.

The regularized crack surface functional, which characterizes phase field methods (PFM), helps to overcome operative difficulties for complex crack topologies in engineering structures. Therefore, this approach is widely used in the failure analysis of structures. Nguyen-Thanh et al. [10] propose a novel higher-order nonlocal operator method (NOM) based anisotropic phase-field approach to brittle fractures in rock-like materials and polycrystalline materials. Yin et al. [11, 12] proposed innovative frameworks, including meshless peridynamics-based methods for simulating fracture and progressive failure in fiber reinforced composite panels with holes, and a coupled phase-field-adhesive model framework that accurately captures the progressive failure and damage behavior of multiphase microstructures and multi-fiber systems. These studies collectively contribute to the understanding of fracture simulation in fiber reinforced composite panels with holes, providing insights into crack initiation, propagation, and fracture behavior under various conditions. Kumar et al. [13] developed a novel Multi Phase-Field (MPF) model, which relies on the Puck theory of failure for intra-laminar failure at ply level and the Cohesive Zone Model (CZM) for inter-laminar cracking. Nguyen-Thanh et al. [14] also presented a novel higher-order nonlocal operator theory for the phase-field modeling of brittle fracture in anisotropic materials. Incorporating higher order nonlocal operators can enhance the accuracy of the phase-field model by effectively capturing long-range interactions that hold

significance in several engineering materials. Dean et al. [15] proposed a novel phase field model that accounts for the anisotropic response of SFRPs from the theoretical and numerical standpoints.

Furthermore, several researchers have employed alternative approaches to investigate fracture problems. For instance, Tian et al. [16] addressed fracture problems from a multiscale perspective. Shi et al. [17] conducted fracture analysis of planar cracks under chemical-mechanical loading using a linear chemo-elasticity model. Pu et al. [18] introduced a crack softening failure model based on two failure criteria to study dynamic crack propagation in brittle materials. Li et al. [19] developed a multigrid coupling approach of the extended isogeometric–meshfree (XIMF) method and bond-based peridynamics (PD) for static and dynamic fracture problems. The coupling approach exploits the advantages of the XIMF method and PD, including the computational efficiency of the XIMF method and the generality of the PD in dealing with fracture problems. These studies collectively contribute to understanding fracture simulation of composite materials and provide insights into crack initiation, propagation, and fracture behavior under various conditions.

Due to the limitations of manufacturing processes, it is difficult to ensure the controllability of straight fibers in actual products. In addition, the functionality of unidirectional FRC panels is relatively simple and cannot cope with complex and varying external loads. Furthermore, it is necessary to consider the actual bending distribution characteristics of FRCs in order to obtain accurate material performance prediction. By designing curved fibers with varied angles and combining them with various types of matrix, the FRC can be optimized for use in different engineering applications such that the use of their anisotropic properties is maximized [20]. Therefore, the study of curved FRC panels has universal significance [21].

In engineering practice, materials will inevitably be subjected to various forms of impact [22] and thermal loads in certain situations. The process of thermal shock involves an instantaneous change in temperature, which can result in non-uniform stress and strain changes in the material over a short period of time, ultimately leading to crack growth or even complete material failure [23]. Pavan et al. [24] developed a

thermodynamically consistent coupled thermo-mechanical phase-field model for thin-walled structures using fully-integrated solid shell finite elements. The proposed thermo-mechanical phase-field model is equipped with the Enhanced Assumed Strain (EAS) to alleviate Poisson and volumetric locking. This technique is further combined with the Assumed Natural Strain (ANS) method leading to a locking-free thermo-mechanical solid shell phase-field element. Wang et al. [25] implemented a thermoelastic coupling phase field model in Abaqus/Explicit to simulate quasi-static and dynamic fracture of thermoelastic brittle materials. Pasternak [26] established boundary integral equations and a dual boundary element method for fracture in anisotropic thermoelastic solids, demonstrating its effectiveness. Nguyen et al. [27] conducted numerical studies on the thermal-mechanical crack propagation of orthotropic composite materials using the extended finite element method with nodal gradients. They proposed an enrichment approximation method for discontinuous temperature fields in orthogonal anisotropic media with cracks considering the influence of material orientation for the first time.

This paper investigates the fracture behavior of FRC plates with different hole distribution patterns using the phase field method within a finite element implementation. Our numerical investigations are intended to offer reliable theoretical guidance for the structural design of fiber-reinforced composites (FRC). These new insights could facilitate the adoption of FRC panel in practical engineering applications such as structural energy storage devices.

The remainder of the paper is structured as follows. In Section 2, we introduce the theoretical model of the phase field method. In Section 3, we describe in detail the finite element implementation of the phase field model. In Section 4, we presented a parametric study of the FRC panels under different conditions. For this purpose, we employ an FE-based implementation of the present formulation in MATLAB. Some important conclusions that are significant for the FRC structure design and manufacturing are presented in Section 5.

2. Computational model

2.1 Phase-field modeling of fracture

In 1998, Francfort and Marigo proposed a variational principle based on Griffith's theory for brittle fracture [28], using the possible displacement field and set of crack surfaces within a structure as independent variables. The total energy of the structure is defined as the sum of the deformation energy and fracture energy, and the real displacement field and crack surfaces can be obtained by minimizing this energy. In 2000, Bourdin et al. [29] introduced a phase-field modeling, which uses a continuous scalar field to describe cracks. The phase-field modeling transforms the problem of crack initiation and evolution within a structure into an optimization problem of coupling multiple fields to minimize energy, without the need to track the path of the crack.

The parameter $s \subseteq [0,1]$ is introduced to represent the crack state, where s = 0 denotes the intact state and s = 1 represents the complete rupture state. Since damage is primarily caused by tension or shear, this study only investigates such kind of damage. To simplify the problem, a two-phase field model can be used, where one phase field parameter s_f represents the fiber damage state and the other parameter s_m represents the matrix damage state.

A solid region $\Omega \in \mathrm{R}^2$ with a boundary $\partial\Omega$ embedded with an internal fiber crack Γ_f and matrix crack Γ_m. The displacement field is denoted as $\boldsymbol{u}$, and the strain tensor as $\boldsymbol{\varepsilon}$.

The fracture energy can be approximated as

$$\int_{\Gamma} q_c \mathrm{d}\Gamma \approx \int_{\Omega} q_c \xi(s, \nabla s)\, \mathrm{d}\Omega \tag{1}$$

where q_c is the critical energy release rate per unit volume, and $\gamma(\mathrm{d}, \nabla \mathrm{d})$ is the crack surface density function. For isotropic materials, the following form is often adopted:

$$\xi(s, \nabla s) = \frac{1}{2l} s^2 + \frac{l}{2} |\nabla s \cdot \nabla s| \tag{2}$$

The crack surface density function is extended to anisotropic materials by

incorporating a second-order structure tensor:

$$\xi(s,\nabla s)=\frac{1}{2l}s^2+\frac{l}{2}\nabla s\cdot\mathbf{A}\nabla s \tag{3}$$

Here, l is a length scale parameter that determines the width of the smooth transition of the crack. There are primarily two strategies to define l. The first strategy treats l as a material property [30], in terms of $l=\frac{27}{256}\frac{Eq_c}{\sigma_s^2}$ (where E represents the Young's modulus, and σ_s is the material strength). The second strategy treats l as a numerical parameter, and its value should be at least twice the size of the mesh length [31].

$\mathbf{A}$ is a second-order structure tensor, given by $\mathbf{A}=\mathbf{A}_m-\vartheta\cdot\mathbf{A}_f$, where ϑ is a penalty parameter. Two structure tensors based on fiber failure $\mathbf{A}_f$ and matrix failure $\mathbf{A}_m$ are introduced. $\mathbf{e}_1$ represents the main direction 1 of the material with high fracture toughness and strength, while $\mathbf{e}_2$ represents the direction perpendicular to $\mathbf{e}_2$.

$$\mathbf{A}_f=\mathbf{e}_2\otimes\mathbf{e}_2,\ \mathbf{A}_m=\mathbf{e}_1\otimes\mathbf{e}_1 \tag{4}$$

Therefore, the crack surface density function can be expressed as follows:

$$\xi_f\left(s_f,\nabla s_f\right)=\frac{1}{2l_f}s_f^2+\frac{l_f}{2}\nabla s_f\cdot\mathbf{A}_f\nabla s_f \tag{5}$$

$$\xi_m\left(s_m,\nabla s_m\right)=\frac{1}{2l_m}s_m^2+\frac{l_f}{2}\nabla s_f\cdot\mathbf{A}_m\nabla s_m \tag{6}$$

The strain energy density can be decomposed into two parts, the contribution from the fibers denoted as ϕ_f and the contribution from the matrix denoted as ϕ_m [32]:

$$\phi(\boldsymbol{\varepsilon})=\phi_f(\boldsymbol{\varepsilon})+\phi_m(\boldsymbol{\varepsilon}) \tag{7}$$

The potential energy density function can be written in the following form:

$$\Phi\left(\boldsymbol{u},s_f,s_m,\nabla s_f,\nabla s_m\right)=\int_\Omega\phi\left(\boldsymbol{\varepsilon}(\boldsymbol{u}),s_f,s_m\right)d\Omega+\sum_{i=f,m}\int_\Omega G_{c,i}\xi_i\left(s_i,\nabla s_i\right)d\Omega \tag{8}$$

The main objective of this study is the fracture behavior of FRC panels, with a

focus on their fracture behavior under tension and shear conditions. To avoid mutual penetration of crack surfaces and to simulate the degradation of material properties, it is necessary to decompose the elastic strain energy density. For isotropic materials, two methods have been proposed to decompose the strain tensor, namely spectral decomposition [33] and hydrostatic-deviatoric decomposition [34], which can be used to address this issue. The elastic potential energy density can be decomposed into positive and negative parts based on the sign of the principal strain vector:

$$\phi_f\left(\boldsymbol{\varepsilon}, s_f\right)=\frac{1}{2} g\left(s_f\right) \phi_f^{+}+\phi_f^{-} \tag{9}$$

$$\phi_m\left(\boldsymbol{\varepsilon}, s_m\right)=\frac{1}{2} g\left(s_m\right) \phi_m^{+}+\phi_m^{-} \tag{10}$$

$$g_i\left(s_i\right)=\left(1-s_i\right)^2+k, i=f, m \tag{11}$$

According to the Clausius-Duhem inequality and the fact that s_f and s_m are independent of each other, a series of derivations lead to the following expressions for s_f and s_m:

$$2\left(1-s_f\right) \phi_f^{+}-G_{c, f}\left[\frac{s_f}{l_f}-l_f \nabla s_f \cdot \mathbf{A}_f \nabla s_f\right]=0 \tag{12}$$

$$2\left(1-s_m\right) \phi_m^{+}-G_{c, m}\left[\frac{s_m}{l_m}-l_m \nabla s_m \cdot \mathbf{A}_m \nabla s_m\right]=0 \tag{13}$$

The strong form for the phase-field problem can be obtained as follows:

$$2\left(1-s_f\right) \frac{\phi_f^{+}}{G_{c, f}}-\left[\frac{s_f}{l_f}-l_f \nabla s_f \cdot \mathbf{A}_f \nabla s_f\right]=0 \text{ in } \Omega, \quad \nabla s_f \cdot \mathbf{n}=0 \text{ on } \partial \Omega; \tag{14}$$

$$2\left(1-s_m\right) \frac{\phi_m^{+}}{G_{c, m}}-\left[\frac{s_m}{l_m}-l_m \nabla s_m \cdot \mathbf{A}_m \nabla s_m\right]=0 \text{ in } \Omega, \quad \nabla s_m \cdot \mathbf{n}=0 \text{ on } \partial \Omega \tag{15}$$

2.2 Coupled phase field modeling of thermal-deformation-fracture

The deformations in this article are all small deformations, and the strain tensor is

represented as the elastic strain tensor ε_e and the thermal strain tensor ε_θ.

$$\varepsilon = \varepsilon_e + \varepsilon_\theta \tag{16}$$

Where ε_θ is directly proportional to the temperature, that is,

$$\varepsilon_\theta = \alpha\theta\mathbf{I} \tag{17}$$

Where α is linear expansion coefficient of the material, θ is temperature and I is the identity tensor. The heat flux $\mathbf{J}$ is directly proportional to the temperature gradient $\nabla\theta$:

$$\mathbf{J} = -k\nabla\theta, k = g(\mathrm{s})k_0 \tag{18}$$

Where k is thermal conductivity of the material, and $g(s)$ is the degenerate function. According to the principle of energy conservation, the energy in the system is represented as

$$\omega^k + \omega^i - \omega^e - \omega^h = 0 \tag{19}$$

where ω^k is the rate of change of kinetic energy, ω^i is the rate of change of internal energy, ω^e is the power of external forces, and ω^h is the power provided by the heat source and heat flux.

Assuming that only the heat generated by the heat source and external heat flux contributes to the temperature change of the object, the heat generated by deformation and fracture can be ignored. The rate of change of internal energy can be divided into the following three parts:

$$\omega^i = \dot{\Psi}_e + \dot{\Psi}_\Gamma + \dot{\Psi}_\theta \tag{20}$$

where $\dot{\Psi}_e$ is the rate of change of elastic potential energy caused by the temperature change of the object, $\dot{\Psi}_\Gamma$ is the rate of change of crack surface energy, and $\dot{\Psi}_\theta$ is the rate of change caused by the temperature.

$$\dot{\Psi}_\theta(\dot{\theta}) = \int_\Omega \rho c \dot{\theta}\,\mathrm{d}V \tag{21}$$

where ρ and c are the material's mass density and specific heat, respectively. According to the classical Griffith theory, the crack surface energy can be calculated by

the critical energy release rate J integral of the crack surface

$$\begin{aligned}
&\Psi_{\Gamma}(\Gamma)=\int_{\Gamma} G_c \mathrm{d}S \approx \int_{\Omega} G_c\left[\frac{s^2}{2l_0}+\frac{l_0}{2}|\nabla s|^2\right]\mathrm{d}V \\
&\Psi_e=\int_{\Omega}\psi_e \mathrm{d}V \\
&\dot{\psi}_e=\sigma:\dot{\varepsilon}_e-2(1-s)\psi_{e0}\dot{s}
\end{aligned} \tag{22}$$

where ψ_{e0} is represented as

$$\psi_{e0}=\frac{1}{2}\varepsilon_e:\mathbf{C}_0:\varepsilon_e \tag{23}$$

Obtain the strong form of the control equation

$$\begin{aligned}
\rho c\dot{\theta}+\nabla\cdot\mathbf{J}&=\gamma \quad \text{in } \partial\Omega, \\
\nabla\cdot\boldsymbol{\sigma}&=\rho\dot{\mathbf{v}} \text{ in } \Omega, \\
\frac{G_c}{l_0}\left[d-l_0^2\nabla^2 s\right]&=2(1-s)\psi_{e0} \text{ in}\Omega, \\
\theta&=\bar{\theta} \quad \text{on } \partial\Omega_{\theta}, \\
\mathbf{J}\cdot\mathbf{n}&=\bar{J} \text{ on } \partial\Omega_{\mathbf{J}}, \\
\mathbf{v}&=\bar{\mathbf{v}} \quad \text{on } \partial\Omega_{\mathbf{v}}, \\
\boldsymbol{\sigma}\cdot\mathbf{n}&=\bar{\mathbf{t}} \quad \text{on } \partial\Omega_{\mathbf{t}}, \\
\nabla s\cdot\mathbf{n}&=0 \quad \text{on } \partial\Omega.
\end{aligned} \tag{24}$$

The initial conditions are as follows

$$\begin{aligned}
\theta(\mathbf{x},t)&=\theta_0(\mathbf{x}) \quad \text{in } \Omega, \\
\mathbf{u}(\mathbf{x},t)&=\mathbf{u}_0(\mathbf{x}) \quad \text{in } \Omega, \\
\mathbf{v}(\mathbf{x},t)&=\mathbf{v}_0(\mathbf{x}) \quad \text{in } \Omega.
\end{aligned} \tag{25}$$

2.3 Modeling the fiber orientation and trajectory in FRCs

In this paper, we use the periodic form of linear orientation fiber paths [35]. The selection of fiber angles follows the mathematical formula below. The fiber trajectory is shown in Figure 1.

$$\theta(x)=\begin{cases}\theta_0+2(T_1-T_0)\left|\dfrac{x'-iL}{L}\right|+T_0, & -\dfrac{L}{2}+iL\le x'\le\dfrac{L}{2}+iL \\ \theta_0+2(T_1-T_0)\left|\dfrac{x'+iL}{L}\right|+T_0, & -\dfrac{L}{2}-iL\le x'\le\dfrac{L}{2}-iL\end{cases}, i\in(0,1,2,\cdots) \tag{26}$$

where θ_0 is the initial local coordinate angle, T_0 is the initial elevation angle of the fiber, T_1 is the final elevation angle, and L is the projected length of periodic

fibers in local coordinates. The material parameters are shown in Table 1.

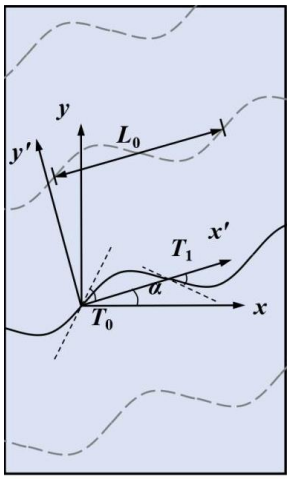

Figure 1 Schematic illustration of curved fiber trajectory

3. Finite Element Method (FEM)

The displacement u and damage parameters s_f, s_m are generally expressed using interpolation functions and corresponding nodal values of displacement and phase field. Each element is defined by its corresponding nodes.

$$\boldsymbol{u} = \boldsymbol{N}^u \boldsymbol{u}^e = \sum_{i=1}^{n_q} \boldsymbol{N}_i^u \boldsymbol{u}_i^e \tag{27}$$

$$s_f = \boldsymbol{N}^s s_f^e = \sum_{i=1}^{n_q} \boldsymbol{N}_{f,i}^s s_{f,i}^e \tag{28}$$

$$s_m = \boldsymbol{N}^s s_m^e = \sum_{i=1}^{n_q} \boldsymbol{N}_{m,i}^s s_{m,i}^e \tag{29}$$

where $\boldsymbol{N}^u$ and $\boldsymbol{N}^s$ are interpolation matrices of shape functions, and in this paper, both the displacement and phase field damage parameters are represented by the same shape functions. $\boldsymbol{u}^e$ and s_f^e, s_m^e are the nodal values of displacement and phase field damage parameters within the element, n_p represents the number of nodes within the element, and $\boldsymbol{B}^{\boldsymbol{u}}$ $\boldsymbol{B}^{s_i}$ $(i = f, m)$ are differential matrices of displacement and phase field, respectively.

$$\boldsymbol{\varepsilon} = \boldsymbol{B}^u \boldsymbol{u}^e \tag{30}$$

$$\nabla s_f = \boldsymbol{B}^{s_f} s_f^e \tag{31}$$

$$\nabla s_m = \boldsymbol{B}^{s_m} s_m^e \tag{32}$$

The governing equation (Eq. 22) is derived based on the weak form, where $\boldsymbol{t}$ represents the external force vector. To avoid unphysical crack closure, a maximum history function $M_i (i = f, m)$ is introduced, as described in the reference [36].

$$\boldsymbol{R}_u = \int_\Omega \boldsymbol{B}^u \boldsymbol{\sigma} d\Omega - \int_\Omega \boldsymbol{N}^u \boldsymbol{t} d\Omega \tag{33}$$

$$\boldsymbol{R}_f = -\int_\Omega \left\{ \left[2\left(1 - s_f\right) M_f - \frac{s_f}{l_f} \right] \boldsymbol{N}^s - l_f \cdot \boldsymbol{B}^{s_f} \cdot \mathbf{A}_f \cdot \nabla s_f \right\} d\Omega \tag{34}$$

$$\boldsymbol{R}_m = -\int_\Omega \left\{ \left[2\left(1 - s_m\right) M_m - \frac{s_m}{l_m} \right] \boldsymbol{N}^s - l_m \cdot \boldsymbol{B}^{s_m} \cdot \mathbf{A}_m \cdot \nabla s_m \right\} d\Omega \tag{35}$$

The finite element discretization is introduced as described above, where $\boldsymbol{K}$ represents the stiffness matrix, $\boldsymbol{K}_{s_f}$ and $\boldsymbol{K}_{s_m}$ represent the phase-field matrix. The phase-field scalar $s_{f,0}$, $s_{m,0}$ and the maximum history function $M_i (i = f, m)$ are initialized for each node element, and the node displacement $u_0 = 0$ is set. In each iteration, $u_n = u_{n-1}$, $s_{f,n} = s_{f,n-1}$, and $s_{m,n} = s_{m,n-1}$ are solved using a staggered iteration algorithm to obtain the algebraic equation system as follows:

$$\boldsymbol{K}\left(\boldsymbol{u}_n, \boldsymbol{s}_{f,n}, \boldsymbol{s}_{m,n}\right) \boldsymbol{u}_{n+1} = \boldsymbol{F}_{u,n+1} \tag{36}$$

$$\boldsymbol{K}_{s_f}\left(\boldsymbol{u}_{n+1}, \boldsymbol{s}_{f,n}\right) \boldsymbol{s}_{f,n+1} = \boldsymbol{F}_{s_f,n+1} \tag{37}$$

$$\boldsymbol{K}_{s_m}\left(\boldsymbol{u}_{n+1}, \boldsymbol{s}_{m,n}\right) \boldsymbol{s}_{m,n+1} = \boldsymbol{F}_{s_m,n+1} \tag{38}$$

Generally, a high degree of precision in discretizing the computing domain is required when employing the phase field technique. This paper employs MATLAB software to implement the study's code with full quantization. The four nodes quadrilateral isoparametric element with a four-point Gauss quadrature rule is used in this study.

Algorithm 1: Solution Procedure for the Phase Field Method

Initialize $\boldsymbol{u}$, $\mathbf{s}_f$, $\mathbf{s}_m$, $u_{eps}=10^{-4}$, $s_{eps}=10^{-3}$, k_{max}
For n = 1 to ntotal (loop loading steps)
    k = 0;
    While $\boldsymbol{u}^e > u_{eps}$ or $\mathbf{s}^{e,f} > d_{eps,f}$ or $\mathbf{s}^{e,m} > d_{eps,m}$ or $k < k_{max}$
        Update integration counter: k = k+1;
        Compute $\boldsymbol{u}^k$ using Eq. (27);
        Compute $\mathbf{s}^{k,f}$ using Eq. (28);
        Compute $\mathbf{s}^{k,m}$ using Eq. (29);
        Evaluate the residuals $\boldsymbol{u}^e = \boldsymbol{u}^k - \boldsymbol{u}^{k-1}$, $\mathbf{s}^{e,f} = \mathbf{s}^{k,f} - \mathbf{s}^{k-1,f}$, $\mathbf{s}^{e,m} = \mathbf{s}^{k,m} - \mathbf{s}^{k-1,m}$;
    End
    Set $\boldsymbol{u}_n = \boldsymbol{u}^k$, $\mathbf{s}_{n,f} = \mathbf{s}^{k,f}$, $\mathbf{d}_{n,m} = \mathbf{s}^{k,m}$;
End

4. Results and discussion

The presence of circular holes in FRC panels may cause stress concentration and fatigue failure, which can affect the safety and stability of the structure. Therefore, comprehensive fracture analysis is of practical engineering significance for such FRC panels. In practical engineering applications such as structural energy storage devices, the number and size of circular holes could affect the stress, strength and integrity of the composite structure. For example, the wing surface of an aircraft often has a large number of holes, and the number and size of these holes directly affect the weight and performance of the aircraft. Performing fracture finite element analysis on FRC panels with different numbers and distributions of circular holes can evaluate the structural bearing capacity under complex loads and improve their reliability. In detail, based on different engineering requirements, the distribution and shape of the holes can be optimized to achieve better structural performance and effectiveness.

4.1 Simulation of FRC panels with holes

Firstly, we conduct convergence analysis to determine the optimal mesh size. Here, we use a model of FRC panels with holes. Structure I is a thin plate (5mm × 5mm), with 16 holes evenly distributed on the plate (see Figure 2). Each hole has a radius of 0.2mm, and the horizontal and vertical distances between the centers of the circular holes are 1mm. At the bottom edge we apply a fixed constraint on it to limit its

displacement, and at the top edge we apply a displacement increment, which value is denoted as $\Delta u = 1\times10^{-4}$ mm . By dividing the mesh into different sizes, the convergence of the algorithm is investigated.

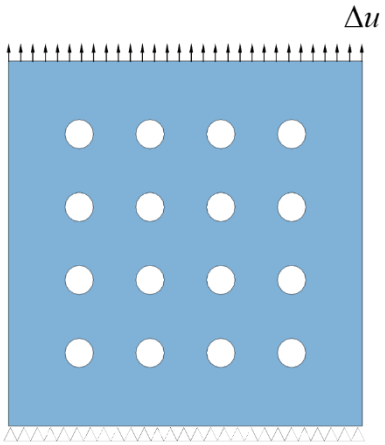

Figure 2 Schematic illustration of structure I

The material parameters are shown in Table 1.

Table 1 Carbon reinforced epoxy HTA/6376 material parameters [37, 38]

Parameter	Value	Unit
Longitudinal modulus	114.8	GPa
Transverse modulus	11.7	GPa
In-plane shear modulus	9.66	GPa
Major Poisson's ratio	0.21	-
Longitudinal fracture energy	106.3	N/mm
Transverse fracture energy	0.2774	N/mm
In-plane shear fracture energy	0.7879	N/mm

For our mesh convergence study, we employed five different mesh sizes as listed in Table 2.

Table 2 Mesh information

Type	Mesh size for circular hole (mm)	Mesh size for edge (mm)
a	0.1	0.05

b	0.05	0.05
c	0.04	0.05
d	0.02	0.05
e	0.01	0.05

Setting the fiber orientation angle to 45°, five sets of results are obtained as shown in Figure 3. The results indicate that as the mesh density increases, the displacement-load curve becomes identical. Groups d and e differ in the number of meshes by almost two times, but their curves are almost the same. Based on the crack patterns in Figure 4, it can be seen that the data from group a is obviously distorted compared to the other four groups. Therefore, in subsequent calculations, the mesh division rule of group d can be used.

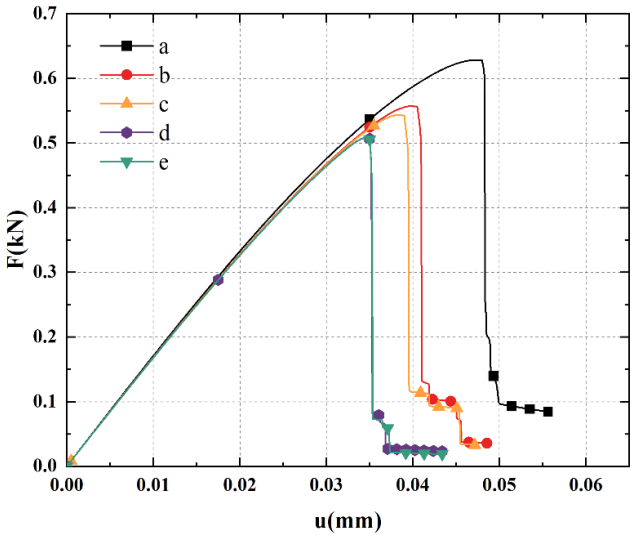

Figure 3 Displacement-load curves at 45° inclination for unidirectional FRC panels

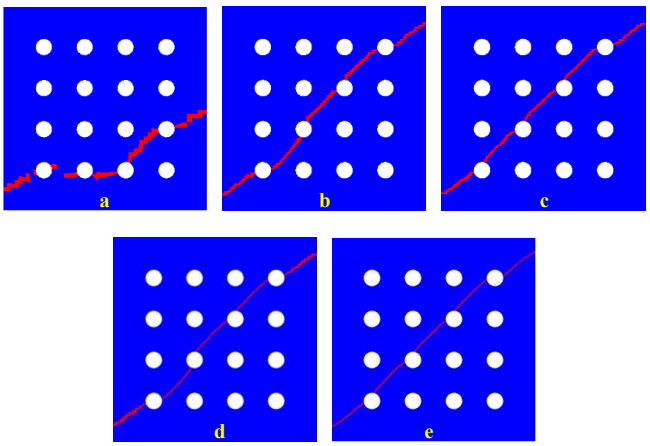

Figure 4 Fracture diagram of unidirectional FRC panels with 45° inclination

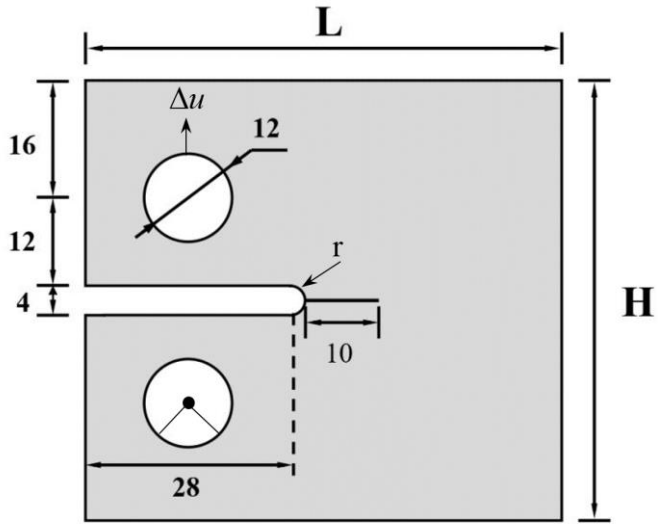

Figure 5 A schematic of the model geometry of the tensile test comparison. All dimensions are given in mm.

Table 3 Tensile test model material parameters [39]

Parameter	Value	Unit
Longitudinal modulus	61.4	GPa
Transverse modulus	61.4	GPa
In-plane shear modulus	3.782	GPa
Major Poisson's ratio	0.042	-
Longitudinal fracture energy	65.4	N/mm
Transverse fracture energy	65.4	N/mm
In-plane shear fracture energy	98.1	N/mm

To evaluate the accuracy and predictive capability of the proposed phase-field model, we employed the isotropic tensile test [39] as a benchmark. The geometric parameters of the model are shown in Figure 5, where $L = 68$ mm, $H = 60$ mm, $r = 0.2$ mm. The length of the pre-crack is taken as 10 mm. Other relevant mechanical parameters are given in Table 3.

The initial crack region is meshed based on the initial geometry (Figure 5), and refinement is performed in the expected crack propagation region. The nodes around the lower circular hole are fixed, while the nodes around the upper circular hole are subjected to displacement. The value of the displacement increment is adopted as $\Delta u = 3\times10^{-5}$ mm. By comparing the results with experimental data (as shown in Figure 6), the two curves were found to be consistent, thus demonstrating the effectiveness of the proposed algorithm.

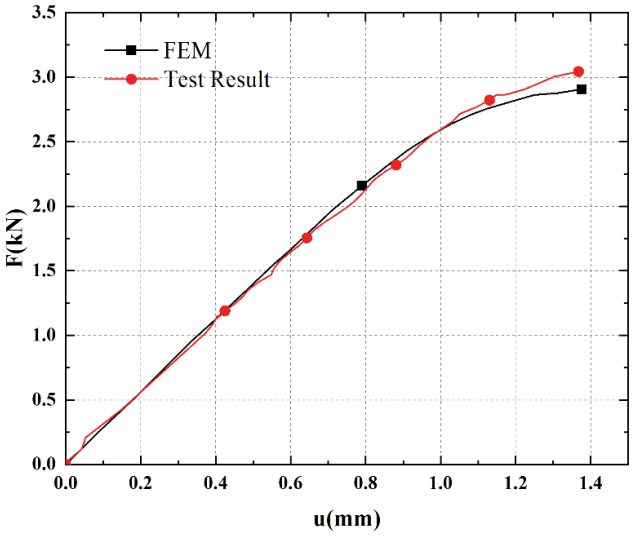

Figure 6 Displacement-load curves of experimental data and our phase field model

We established three different structures of plates with the same hole area as shown in Figure 7: Structure I with 4×4 holes, Structure II with 2×2 holes, and Structure III with 1×1 hole. The hole radius in Structure I is 0.2 mm, in Structure II is 0.4 mm, and in Structure III is 0.8 mm, with a ratio of 1:2:4. The hole number ratios are 16:4:1, respectively, ensuring equal hole area and uniform distribution throughout the plate for all three structures. The material parameters are shown in Table 1. The

boundary conditions are shown in Figure 7. The displacement increment $\Delta u = 1\times10^{-4}$ mm is adopted.

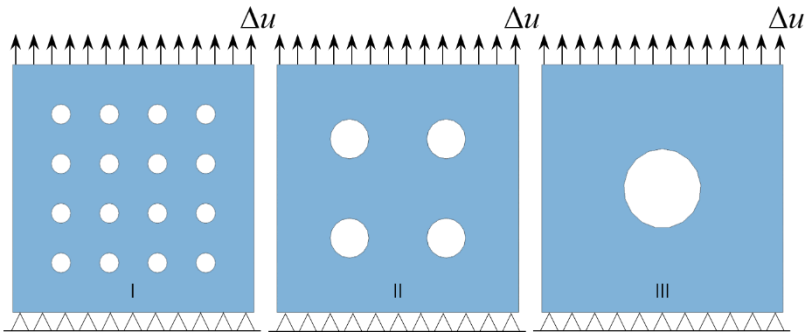

Figure 7 Schematic diagrams of a FRC structure with three different holes configurations

To investigate the influence of hole size on the mechanical properties of the FRC structures (Figure 7), we performed unilateral tensile loading simulations, with the fiber angle set at 45°. As shown in Figure 8, the higher the number of holes, the larger the load the unidirectional FRC panels can withstand. For a plate with a fixed total hole area, as the number of holes increases, the area of each hole decreases, leading to a reduction in the effective cross-sectional area. However, with more holes densely distributed on the plate, the load can be more evenly dispersed onto the holes, relieving stress concentration around the holes. Moreover, an increase in the number of holes increases the surface area of the plate, which enables the load to be better dispersed and reduces local stress concentration when bearing the load. Although the area of each hole decreases, the maximum load-carrying capacity of the plate increases with an increase in the number of holes.

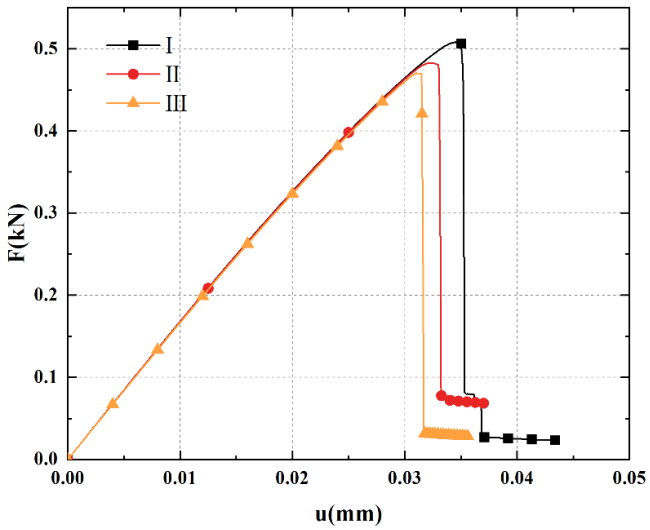

Figure 8 Displacement-load curves for three different structures

Furthermore, to compare the effect of different fiber angles on the mechanical properties of the plates, we perform uniaxial tensile calculations on unidirectional FRC panels with fiber angles θ of 30°, 45°, and 60°. Structure I is chosen for the calculation.

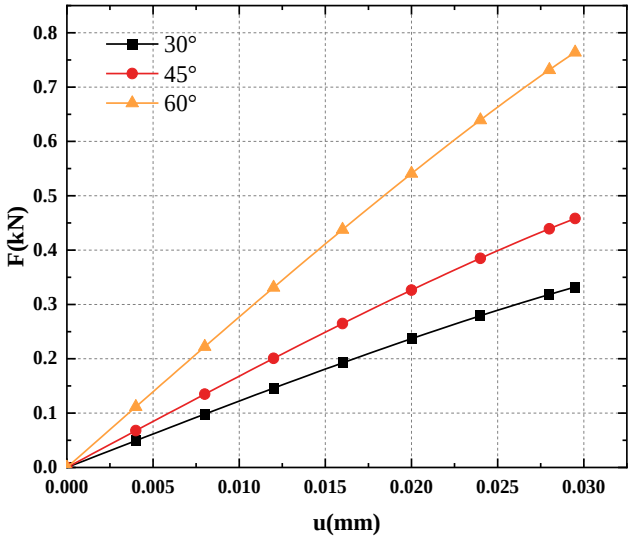

Figure 9 Displacement-load curves for unidirectional FRC panels at different inclination angles

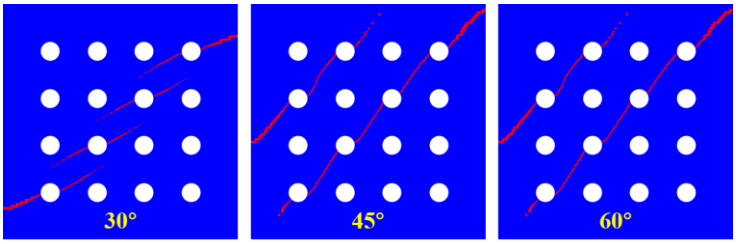

Figure 10 Fracture pattern at different fiber angles in unidirectional FRC panels

As the fiber angle increases, the angle between the fiber and the loading direction decreases. Based on the calculation results shown in Figure 9, we can draw an important conclusion that the bearing capacity of unidirectional FRC panels increases with the increase of fiber angle at the same displacement. From an energy perspective, as shown in Figure 10, when the fiber angle increases, the crack length also increases, resulting in more energy consumption. However, due to the higher toughness of the material, it can withstand more loads before complete fracture, thus demonstrating a higher load-bearing capacity. Therefore, it is concluded that the fiber angle has a significant effect on the bearing capacity of the material and should be fully considered in the material design and application process.

4.2 Simulation of curved FRC panels with holes

In order to model the curved FRC panels, the fiber orientation description in Section 2.3 will be employed. Here, the parameters $[T_0, T_1]$ are used to denote the properties of curved fibers characteristics. For structure III, two fiber angles, namely [45,0] and [60,0], were considered. The boundary conditions are shown in Figure 7. Our numerical results, as presented in Figures 11 and 12, show that the maximum load-carrying capacity of the structure increases with increasing fiber elevation angle. However, the load-carrying capacity of the structure is rapidly lost once the structure fails. Since the elastic energy is a quadratic function of stress, the elastic energy exhibits nonlinear growth with increasing load. As the displacement increases, the elastic energy grows faster, while the energy required to generate a crack surface remains constant. The release of more energy increases the number of crack surfaces, thereby increasing the crack propagation rate. As the crack grows, the stress on the remaining effective connecting parts of the material increases. Although the overall elastic energy decreases, the elastic energy density increases, requiring the release of more elastic energy. When the critical point is reached, even small displacements will generate a large number of crack surfaces, which explains why the load drops quickly after reaching its peak. Only a few cracks are observed in the crack pattern at the highest load point.

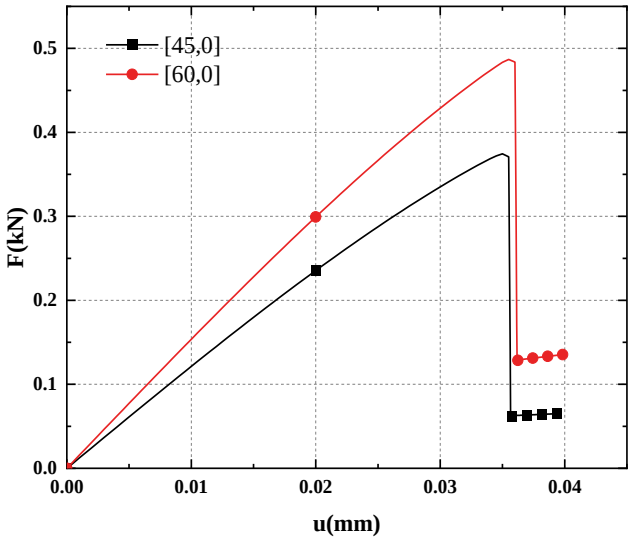

Figure 11 Displacement-load curves of curved FRC panels at different angles

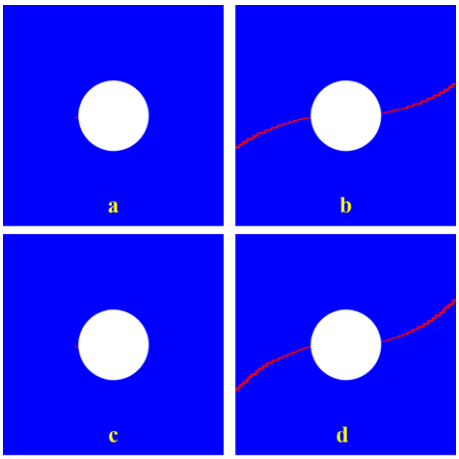

Figure 12 Fracture pattern of curved FRC panels under uniaxial loading at different inclinations. **a** crack pattern at the maximum load for [45,0] orientation, **b** crack pattern at complete failure for [45,0] orientation, **c** crack pattern at the maximum load for [60,0] orientation, **d** crack pattern at complete failure for [60,0] orientation

After comparing the displacement-load curves as shown in Figure 13 and crack patterns of curved FRC panels with [0,45] and [45,0] angles as shown in Figure 14, it was found that under the same elevation angle conditions, the curved FRC panels with a larger initial elevation angle and smaller final elevation angle has a higher maximum load compared to the plate with a smaller initial elevation angle and larger final elevation angle. In addition, cracks propagate in the fiber direction of the plate.

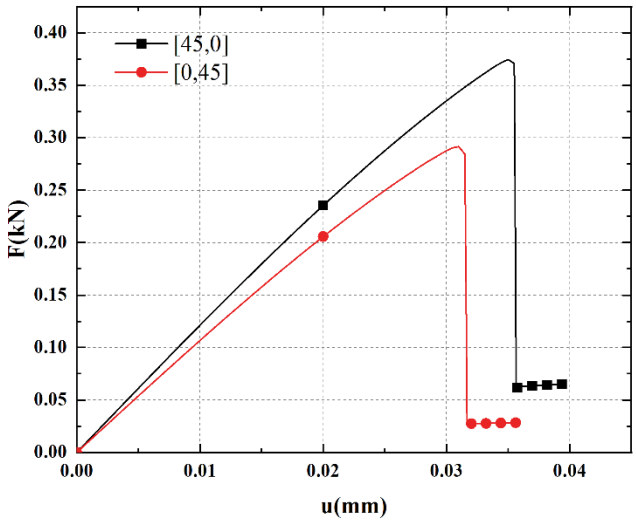

Figure 13 Displacement-load curves for curved FRC panels at different inclination angles

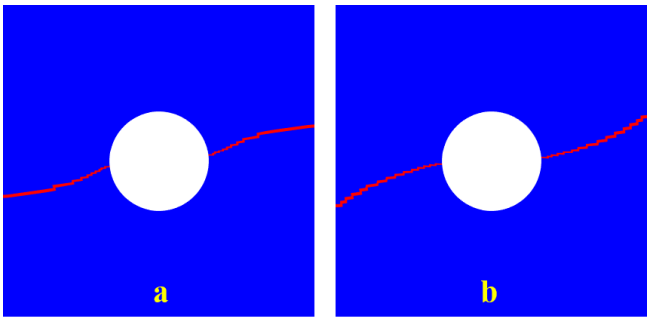

Figure 14 **a** Fracture pattern at complete failure of [0,45] orientation, and **b** Fracture pattern at complete failure of [45,0] orientation.

Upon comparing the 45° unidirectional fiber and the [45,0] curved fiber, it was observed that the maximum load of the former is greater than that of the latter as shown in Figure 15. However, under the same displacement, the load of the curved fiber is smaller. As cracks propagate along the fibers, the crack initiation angle in the unidirectional fiber is closer to the load direction than that of the curved fiber. This means that the 45° unidirectional FRC panels can withstand a larger load due to the smaller initial crack angle with respect to the load direction. Additionally, it can be seen from the displacement-load curve that the curved FRC panels with [45,0] angle can withstand more displacement load than the 45° unidirectional FRC panels. This is attributed to the lower elastic modulus of the 45° unidirectional FRC panels, which results in lower stress around the circular hole. Consequently, the curved FRC panels

with [45,0] angle can withstand more displacement load. Therefore, different FRC panels with varying angles can be selected according to the type of load they need to bear.

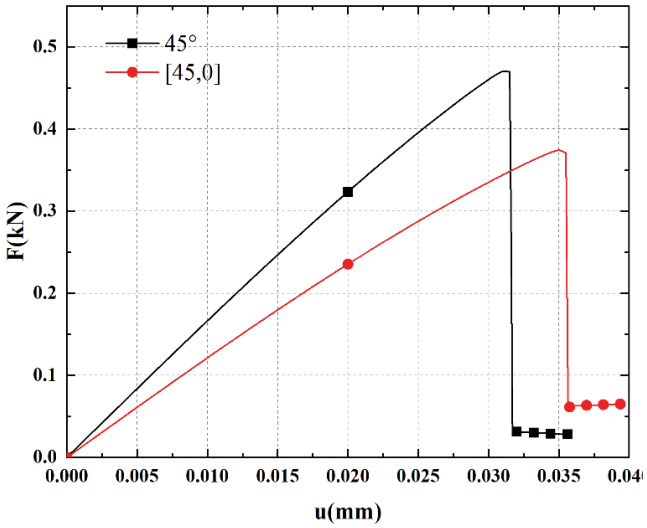

Figure 15 Displacement-load curves of unidirectional FRC panels and curved FRC panels

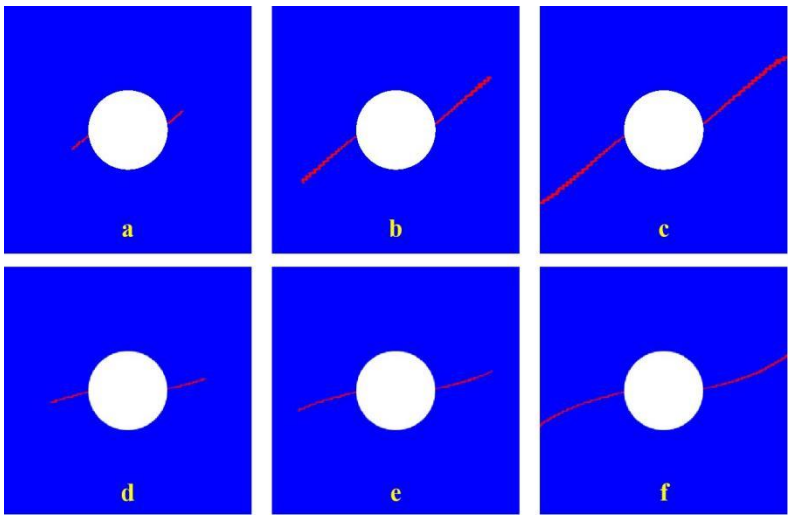

Figure 16 Fracture pattern of unidirectional and woven FRC. a fracture pattern of 45° unidirectional FRC panels at maximum load, b fracture pattern of 45° unidirectional FRC panels at crack extension, c fracture pattern of 45° unidirectional FRC panels at ultima failure, **d** fracture pattern of [45,0] curved FRC panels at maximum load, **e** fracture pattern of [45,0] curved FRC panels at crack extension, and **f** fracture pattern of [45,0] curved FRC panels at ultimate failure

4.3 Simulation of curved FRC panel without holes

The following calculations were performed on a non-perforated curved fiber-reinforced composite (FRC) panel with a pre-crack, as shown in Figure 17, in order to investigate the relationship between their fracture behavior and fiber angles without the influence of holes. We applied a fixed constraint at its bottom edge and a displacement increment of $\Delta u = 1\times10^{-4}$ mm at the top edge; and we added a pre-crack of 0.5 mm at the midpoint of the left edge, as shown in Figure 17. The material parameters are shown in Table 1.

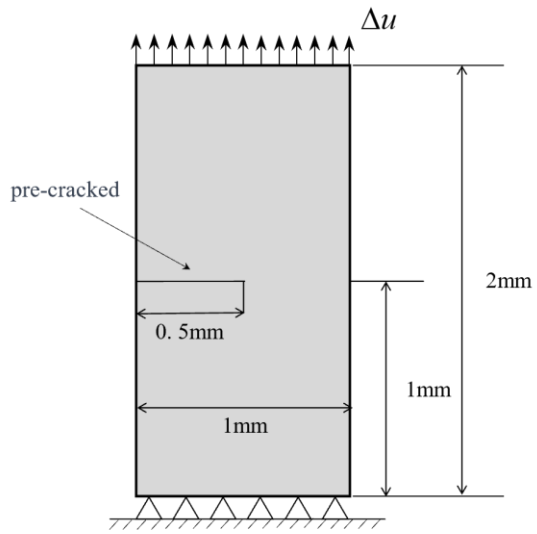

Figure 17 Curved FRC panels with pre-crack

From Figures 18 and 19, it can be seen that the straight fibers can bear more load than the curved fibers. This is because, at the tip of the pre-cracked, the angle of the straight fibers is 60°, while the angle of the curved fibers is 0°. Since the difference in fiber angle at the crack initiation is greater in this data set, it provides a more intuitive representation of the difference in maximum load between the two structures compared to the structure with the hole.

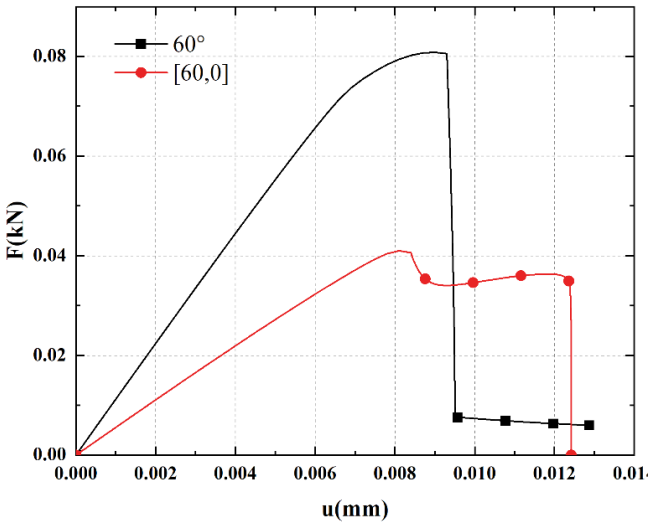

Figure 18 Displacement-load curves for pre-cracked unidirectional and curved FRC panels

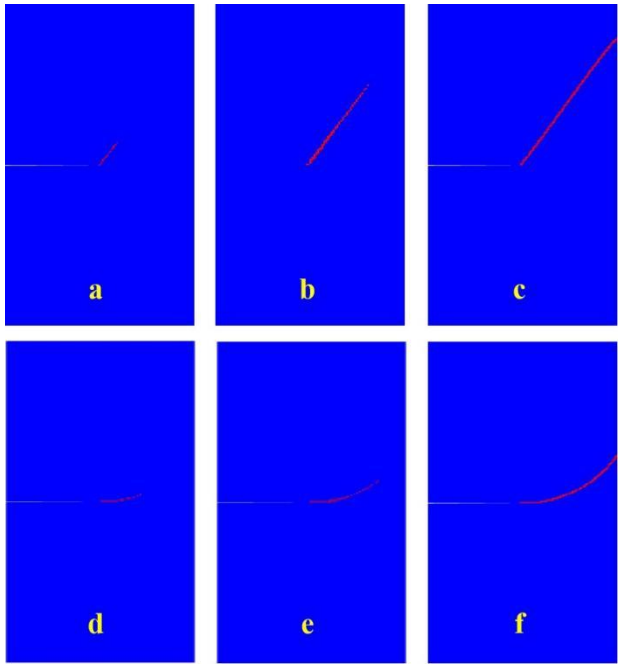

Figure 19 Fracture pattern of unidirectional FRC plates and curved FRC plates with pre-cracked. **a** fracture pattern at the maximum load for 60° in unidirectional FRC panels, **b** fracture pattern at crack extension for 60° in unidirectional FRC panels, **c** fracture pattern at complete fracture for 60° in unidirectional FRC panels, **d** fracture pattern at the maximum load for fiber [60,0] orientation, **e** fracture pattern at crack extension for fiber [60,0] orientation, and **f** fracture pattern at complete failure for fiber [60,0] orientation.

To further investigate the impact of curved fibers at different angles on load, we compared the displacement-load curves at angles of [0,60] and [60,0] in a FRC panels reinforced with pre-cracked. As shown in Figures 20 and 21, it was found that there exists a plateau in the displacement-load curve, whose length is dependent on the fiber angle. In the later stage of crack propagation, i.e., on both sides of the plate, the difference between the two angles lies in the difference in fiber angles on both sides of the plate. Compared with the [0,60] angle, the [60,0] angle has fibers that are closer to the load direction on both sides of the plate. Since cracks propagate along the fiber direction, the variation in crack angle causes the effective connection part (i.e., the projection length of the remaining connection part of the structure on the x-axis) consumed for generating the same length of crack to decrease. Meanwhile, the rate of elastic energy growth slows down relative to the initial stage of crack generation. This situation prevents the generation of a large number of cracks due to displacement changes, thereby providing a buffering effect against structural failure. As the angle approaches the edge, the angle between the edge and the load direction decreases, making the buffering effect more pronounced.

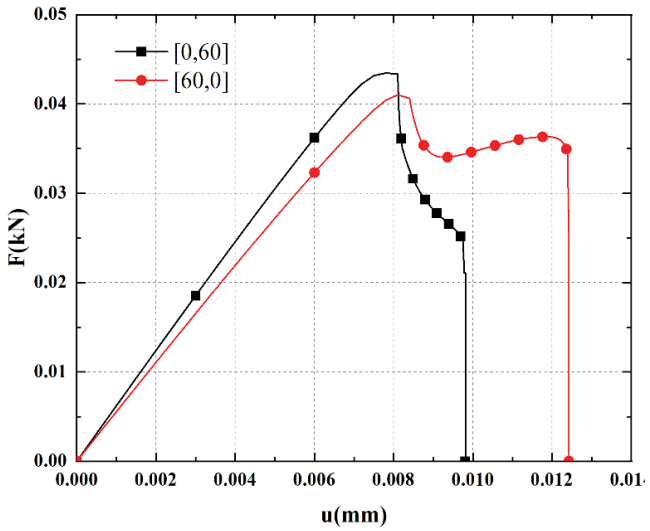

Figure 20 Displacement-load curves of curved FRC panels with pre-crack

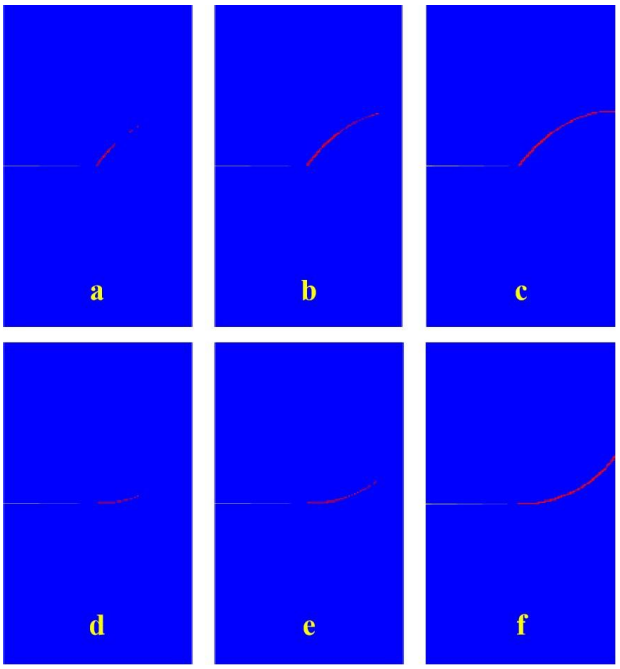

Figure 21 Fracture patterns of curved FRC panels with pre- cracked: **a** fracture pattern at the maximum load for fiber [0,60] orientation, **b** fracture pattern at crack extension for fiber [0,60] orientation, **c** fracture pattern at complete failure for fiber [0,60] orientation, **d** fracture pattern at the maximum load for fiber [60,0] orientation, **e** fracture pattern at crack extension for fiber [60,0] orientation, and **f** fracture pattern at complete failure for fiber [60,0] orientation.

On the other hand, by comparing the load-displacement diagrams of curved fiber panels without circular holes in this section 4.2(as shown in Figures 18 and 20), with the load-displacement diagrams of curved fiber panels with circular holes in Section 4.3(as shown in Figures 11, 13, and 15), we find that the displacement-load curve of FRC panels containing a circular hole, does not exhibit a clear plateau. This is due to the narrow effective connection area caused by the presence of the hole, which leads to a small projection length of the remaining connection area on the x-axis after crack generation. As a result, the elastic energy near the crack tip increases too quickly, making it impossible to achieve balance by generating enough crack surface area, and therefore, an excessive zone does not occur.

4.4 Simulation of shear tests of curved FRC panels

In this section, we investigated the fracture behavior of curved FRC panels under shear force with a displacement increment of $\Delta u = 1\times10^{-4}$ mm. We applied a fixed constraints to the bottom edge and employed the model parameters in Table 1. The schematic diagram is shown in Fig. 22.

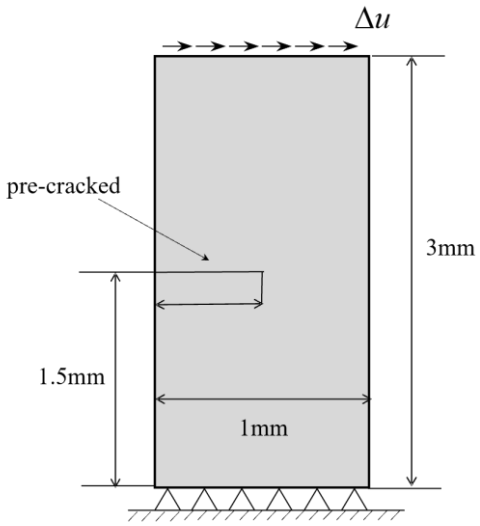

Figure 22 Schematic diagram of the curved FRC plate subject to a shear load

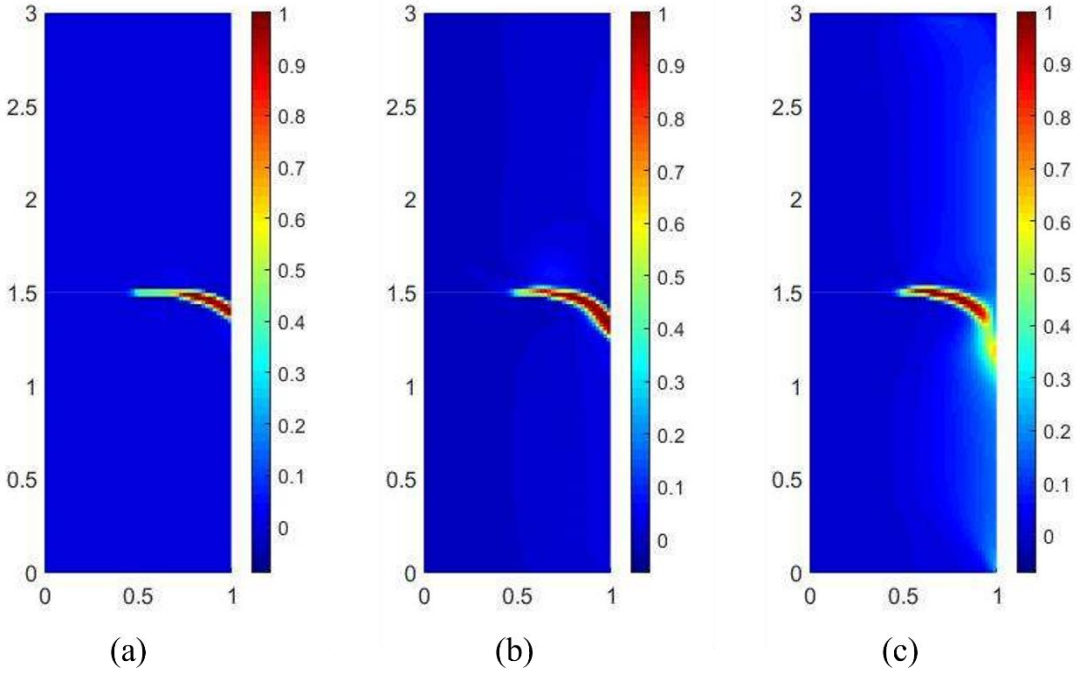

Figure 23 Shear tests of FRC fracture: (a) $T_0 = -30$;(b) $T_0 = -45$;(c) $T_0 = -60$

We calculate this for the cases T_0 = -30°, -45°, and -60°, and the results are shown

in Figure 23. Our results are in agreement with the findings of Pan et al. [35]. Similar to the results presented in Section 4.3 above, we noted that the cracks are also propagated in the direction of the fibers. Interestingly, we observed that, unlike the other two angles, at T_0 = -60°, the cracks in the FRC panel, in addition to expanding along the direction of the fibers, had a tendency to sprout at the right edge of the crack before growing across the panel.

4.5 Simulation of fracture of FRC under thermal shock

This section focuses on the fracture behavior of a glass fiber reinforced composite plate with edge crack under thermal shock loading. The boundary conditions and loading conditions are shown in Fig. 24. The dimensions of the plate are W × L (L = 3W) and there is a pre-crack of length a/W = 0.15 at the edge of the plate, where W = 1mm.

The thermal shock is simulated in a manner similar to the quenching process. The initial temperature is applied to the left edge and allowed to decrease gradually, while the temperatures on the rest of the FRC plate surface are maintained at a constant 290 K throughout the simulation. The initial temperature $T = 290\text{K}$. Other relevant material properties are shown in Table 4.

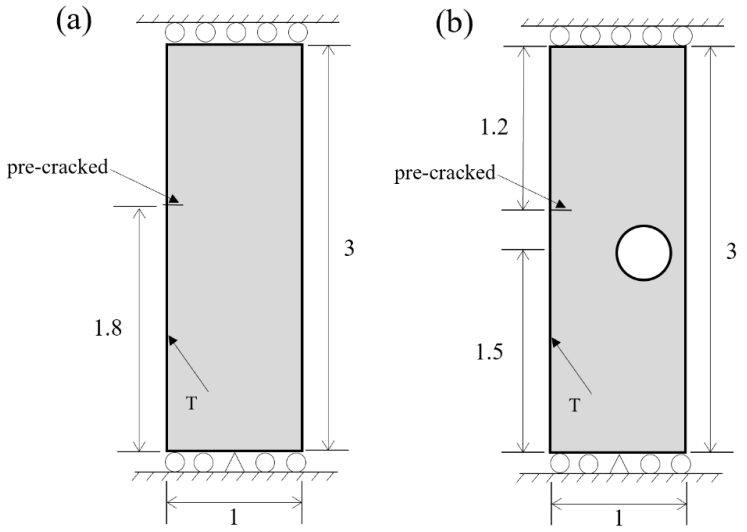

Figure 24 The geometry and boundary conditions of geometry edge crack in rectangular plate:(a) FRC without hole; (b) FRC with hole. All dimensions in mm.

Table 4 Glass/epoxy material parameters [37, 38]

Parameter	Value	Unit
Longitudinal modulus	55	GPa
Transverse modulus	21	GPa
In-plane shear modulus	9.7	GPa
Major Poisson's ratio	0.25	-
Specific heat capacity	106.3	J/KgK
Thermal conductivity	3.46	N/mm
Thermal expansion coefficient	6.3×10^{-6}	K^{-1}

We calculated two types of FRC panels under three fiber angle conditions: 0°, 60°, and -60°.

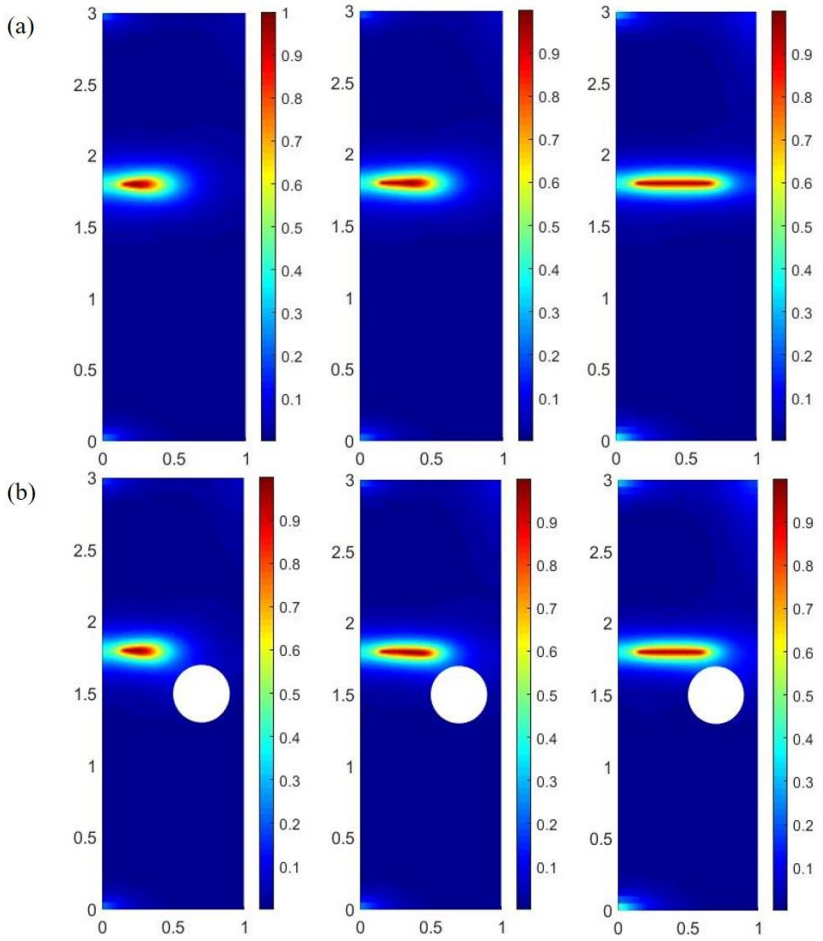

Figure 25 The crack propagation path for the angle of 0° under thermal shock: (a) FRC without hole; (b) FRC with hole.

As shown in Figure 25, it can be seen that at the fiber angle of 0°, the cracks in the two types of FRC panels propagate in a manner similar to when only subjected to mechanical loads, extending along the horizontal axis.

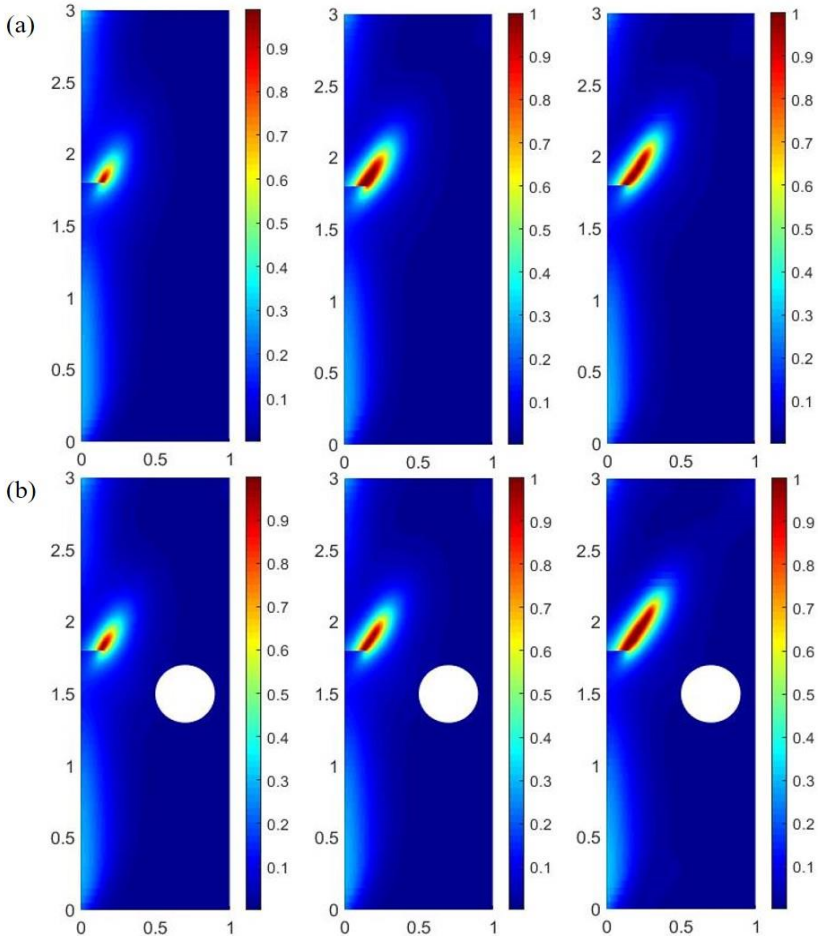

Figure 26 The crack propagation path for the angle of 60° under thermal shock: (a) FRC without hole; (b) FRC with hole.

Figure 26 shows the crack propagation diagram at a fiber angle of 60°. The crack propagation in the non-perforated FRC panel is the same as when subjected to mechanical loads only, with cracks propagating along the direction of fiber laying. However, for the perforated FRC panel at a fiber angle of 60°, cracks no longer strictly propagate along the fiber direction. Instead, the cracks extend upwards at an angle of 52° from the horizontal axis, consistent with the observations by Nguyen et al. [27] under constant heat flux boundary conditions, where cracks extend upwards at a 45° angle from the horizontal axis. At the angle of -60° (as shown in Figure 27), cracks

propagate downwards along the horizontal axis, growing towards the hole at approximately 56°. This phenomenon is considered to be influenced by the presence of holes guiding the crack propagation.

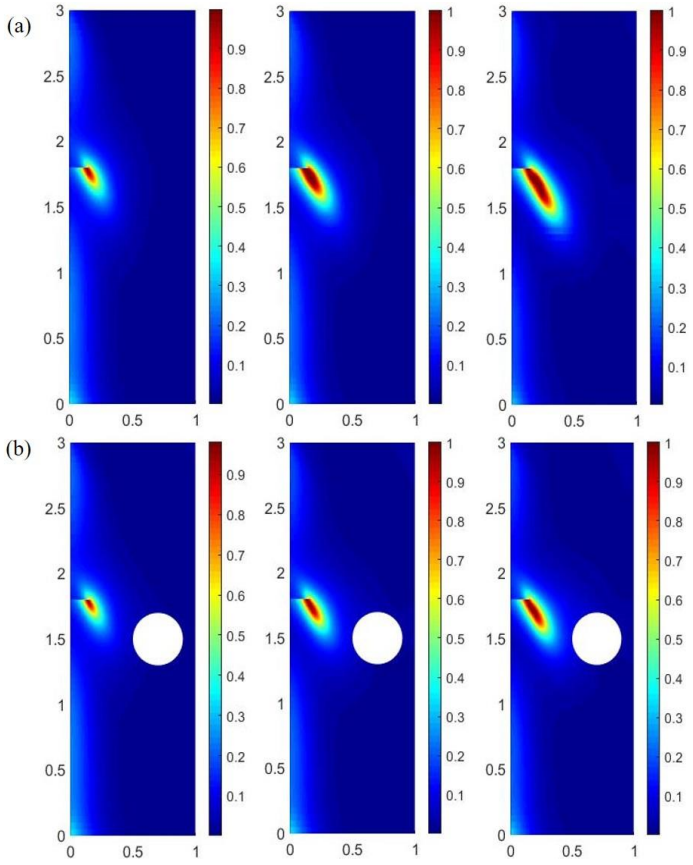

Figure 27 The crack propagation path for the angle of -60° under thermal shock:(a) FRC without hole; (b) FRC with hole.

5. Concluding remarks

This paper applies the phase-field fracture method to investigate the influence of fiber inclination angle, hole size, and other factors on the fracture behavior of FRC. Our numerical results show that:

(a) Regardless of the loading method used or the presence of holes, cracks in fiber-reinforced composites (FRC) tend to propagate along the direction of fiber placement. This is because the stiffness of the fibers exceeds that of the substrate. Consequently, when the material's stiffness is dominant in a particular direction, cracks are likely to develop along that direction.

(b) For unidirectional fiber-reinforced composite (FRC) panels subjected to purely

mechanical loads, increasing the number of holes within a given area results in an enhanced maximum load-carrying capacity of the material plate. This is because an increase in the number of holes leads to a more uniform distribution of the load around the holes, reducing stress concentration around the holes and enabling the plate to better distribute the load when subjected to a load, reducing local stress concentration.

(c) Additionally, the smaller the angle between the fiber direction and the load direction, the higher the load bearing capacity of the FRC structure.

(d) Compared with unidirectional fibers, curved fibers can slow down the rate of structural failure, and do not fail rapidly after the generation of cracks.

We also observed that the fracture behavior of FRC under thermal shock differs from that under purely mechanical loads. Our investigations show that in the absence of holes, when only changing the fiber angle, the crack propagation for both loading conditions is consistent. However, for perforated FRC panels, after changing the fiber angle, crack propagation is influenced by the presence of holes. The direction of crack propagation no longer strictly follows the fiber angle but tends to grow towards the hole.

The overall results indicate that the fiber angle significantly affects the load-bearing capacity of the material, and the impact of the presence or absence of holes on crack propagation in FRC panels should not be overlooked. This can provide theoretical references for the design and application of fiber-reinforced composite materials. Despite the promising results presented in this paper for regularized structures, further studies are required to examine the effect of hole distribution, fiber direction, different reinforcement such as graphene [40, 41] and multiple load scenarios on the fracture behavior of complex FRC structures that are often encountered in practical engineering applications.

Acknowledgments

This work was supported by NSFC under Grant No. 12272182. A.S. Ademiloye and Yang Zhang acknowledge the support provided by the Royal Society through the International Exchange Grant (IES\NSFC\223217).

Data Availability Statement

The authors confirm that the data supporting the findings of this study are available within the article.

References

[1].Bhong, M.; Khan, T. K. H.; Devade, K.; Vijay Krishna, B.; Sura, S.; Eftikhaar, H. K.; Pal Thethi, H.; Gupta, N., Review of composite materials and applications. Materials Today: Proceedings **2023**.

[2].Kim, S. G.; Heo, S. J.; Kim, S.; Kim, J.; Kim, S. O.; Lee, D.; Lee, S.; Kim, J.; You, N.-H.; Kim, M., Ultrahigh strength and modulus of polyimide-carbon nanotube based carbon and graphitic fibers with superior electrical and thermal conductivities for advanced composite applications. Composites, Part B **2022,** 247, 110342.

[3].Chen, Y.; Zhang, L.; Nie, H.; Shao, S.; Sheng, H.; Li, H., Synchronously constructing networked Si3N4 nanowires and interconnected graphene inside carbon fiber composites for enhancing mechanical, friction and anti-ablation properties. J Mater Sci Technol **2023,** 142, 167-175.

[4].Basoglu, M. F.; Kefal, A.; Zerin, Z.; Oterkus, E., Peridynamic modeling of toughening enhancement in unidirectional fiber-reinforced composites with micro-cracks. Compos. Struct **2022,** 297, 115950.

[5].Huang, Y.; Wang, X., On the fracture toughness testing for single-edge notched bend specimen of orthotropic materials. Compos. Struct **2022,** 281, 114970.

[6].Dan, S.; Tarafder, P.; Ghosh, S., Adaptive wavelet-enhanced cohesive zone phase-field FE model for crack evolution in piezoelectric composites. Comput Methods Appl Mech Eng **2022,** 392, 114636.

[7].Tan, W.; Martínez-Pañeda, E., Phase field fracture predictions of microscopic bridging behaviour of composite materials. Compos. Struct **2022,** 286, 115242.

[8].Negi, A.; Soni, A.; Kumar, S., An anisotropic localizing gradient damage approach for failure analysis of fiber reinforced composites. Compos. Struct **2022,** 294, 115677.

[9].Granados, J. J.; Martinez, X.; Barbu, L. G.; Di Capua, D., Fatigue prediction of composite materials, based on serial/parallel mixing theory. Compos. Struct **2022,** 291, 115516.

[10].Nguyen-Thanh, N.; Nguyen-Xuan, H.; Li, W., Phase-field modeling of anisotropic brittle fracture in rock-like materials and polycrystalline materials. Computers & Structures **2024,** 296, 107325.

[11].Yin, B.; Sun, W.; Zhang, Y.; Liew, K., Modeling via peridynamics for large deformation and progressive fracture of hyperelastic materials. Comput Methods Appl Mech Eng **2023,** 403, 115739.

[12].Yin, B.; Akbar, A.; Zhang, Y.; Liew, K., Modeling progressive failure and crack evolution in a randomly distributed fiber system via a coupled phase-field cohesive model. Compos. Struct. **2023,** 313, 116959.

[13].Asur Vijaya Kumar, P. K.; Dean, A.; Reinoso, J.; Paggi, M., A multi phase-field-cohesive zone model for laminated composites: Application to delamination migration. Composite Structures **2021,** 276, 114471.

[14].Nguyen-Thanh, N.; Rabczuk, T., Phase-field modeling of anisotropic crack propagation based on higher-order nonlocal operator theory. International Journal of Solids and Structures **2024,** 289, 112632.

[15].Dean, A.; Reinoso, J.; Jha, N. K.; Mahdi, E.; Rolfes, R., A phase field approach for ductile fracture of short fibre reinforced composites. Theoretical and Applied Fracture Mechanics **2020,** 106, 102495.

[16].Tian, W.-L.; Yang, S.-Q.; Huang, Y.-H.; Dong, Z.-J., Fracture behavior of granite specimen containing a single fissure under uniaxial compression by grain-based model 3D. Acta Mech Sin **2022,** 38 (9), 421510.
[17].Shi, J.; Zhong, Z., Fracture analysis of a plane crack problem under chemo-mechanical loading. Acta Mech Sin **2022,** 38 (7), 421439.
[18].Pu, C.; Yang, X.; Zhao, H.; Chen, Z.; Xiao, D.; Zhou, C.; Xue, B., Numerical study on crack propagation under explosive loads. Acta Mech Sin **2022,** 38 (1), 421376.
[19].Li, W.; Nguyen-Thanh, N.; Zhang, Q.; Du, H.; Li, S.; Zhou, K. J. C. M., A multigrid coupling approach of the extended isogeometric–meshfree method and peridynamics for brittle fracture. **2024,** 73 (2), 427-447.
[20].Maung, P. T.; Prusty, B. G.; Donough, M. J.; Oromiehie, E.; Phillips, A. W.; St John, N. A., Automated manufacture of optimised shape-adaptive compsite hydrofoils with curvilinear fibre paths for improved bend-twist performance. Mar. Struct. **2023,** 87, 103327.
[21].Scheirer, N.; Holland, S. D.; Krishnamurthy, A., Fiber Layup Generation on Curved Composite Structures. Computer-Aided Design **2021,** 136, 103031.
[22].Li, W.; Nguyen-Thanh, N.; Du, H.; Zhou, K., Adaptive phase-field modeling of dynamic brittle fracture in composite materials. Composite Structures **2023,** 306, 116589.
[23].Chu, D.; Li, X.; Liu, Z., Study the dynamic crack path in brittle material under thermal shock loading by phase field modeling. International Journal of Fracture **2017,** 208 (1), 115-130.
[24].Asur Vijaya Kumar, P. K.; Dean, A.; Reinoso, J.; Paggi, M., Nonlinear thermo-elastic phase-field fracture of thin-walled structures relying on solid shell concepts. Computer Methods in Applied Mechanics and Engineering **2022,** 396, 115096.
[25].Wang, T.; Ye, X.; Liu, Z.; Liu, X.; Chu, D.; Zhuang, Z., A phase-field model of thermo-elastic coupled brittle fracture with explicit time integration. Computational Mechanics **2020,** 65 (5), 1305-1321.
[26].Pasternak, I., Boundary integral equations and the boundary element method for fracture mechanics analysis in 2D anisotropic thermoelasticity. Engineering Analysis with Boundary Elements **2012,** 36 (12), 1931-1941.
[27].Nguyen, M. N.; Nguyen, N. T.; Truong, T. T.; Bui, T. Q., Thermal-mechanical crack propagation in orthotropic composite materials by the extended four-node consecutive-interpolation element (XCQ4). Engineering Fracture Mechanics **2019,** 206, 89-113.
[28].Pan, Z.; Zhang, L.; Liew, K., A phase-field framework for failure modeling of variable stiffness composite laminae. Comput Methods Appl Mech Eng **2022,** 388, 114192.
[29].Bourdin, B.; Francfort, G. A.; Marigo, J. J., Numerical experiments in revisited brittle fracture. Journal of the Mechanics and Physics of Solids **2000,** 48 (4), 797-826.
[30].Borden, M. J.; Verhoosel, C. V.; Scott, M. A.; Hughes, T. J.; Landis, C. M., A phase-field description of dynamic brittle fracture. Comput Methods Appl Mech Eng **2012,** 217, 77-95.
[31].Bilgen, C.; Kopaničáková, A.; Krause, R.; Weinberg, K., A detailed investigation of the model influencing parameters of the phase-field fracture approach. GAMM Mitteilungen **2020,** 43 (2), e202000005.
[32].Dean, A.; Kumar, P. A. V.; Reinoso, J.; Gerendt, C.; Paggi, M.; Mahdi, E.; Rolfes, R., A multi phase-field fracture model for long fiber reinforced composites based on the puck theory of failure. Compos. Struct **2020,** 251, 112446.
[33].Miehe, C.; Hofacker, M.; Welschinger, F., A phase field model for rate-independent crack

propagation: Robust algorithmic implementation based on operator splits. Comput Methods Appl Mech Eng **2010,** 199 (45-48), 2765-2778.
[34].Amor, H.; Marigo, J.-J.; Maurini, C., Regularized formulation of the variational brittle fracture with unilateral contact: Numerical experiments. J Mech Phys Solids **2009,** 57 (8), 1209-1229.
[35].Pan, Z. Z.; Zhang, L. W.; Liew, K. M., A phase-field framework for failure modeling of variable stiffness composite laminae. Computer Methods in Applied Mechanics and Engineering **2022,** 388, 114192.
[36].Zhang, P.; Hu, X.; Bui, T. Q.; Yao, W., Phase field modeling of fracture in fiber reinforced composite laminate. Int. J. Mech. Sci. **2019,** 161, 105008.
[37].Bleyer, J.; Alessi, R., Phase-field modeling of anisotropic brittle fracture including several damage mechanisms. Comput Methods Appl Mech Eng **2018,** 336, 213-236.
[38].Pillai, U.; Triantafyllou, S. P.; Essa, Y.; de la Escalera, F. M., An anisotropic cohesive phase field model for quasi-brittle fractures in thin fibre-reinforced composites. Compos. Struct **2020,** 252, 112635.
[39].Rodriguez, P.; Ulloa, J.; Samaniego, C.; Samaniego, E., A variational approach to the phase field modeling of brittle and ductile fracture. Int. J. Mech. Sci. **2018,** 144, 502-517.
[40].Qiu, Y.; Zhang, Y.; Ademiloye, A. S.; Wu, Z., Molecular dynamics simulations of single-layer and rotated double-layer graphene sheets under a high velocity impact by fullerene. Computational Materials Science **2020,** 182, 109798.
[41].Zhang, Y.; Qiu, Y.; Niu, F.; Ademiloye, A. S., Molecular dynamics simulation of perforation of graphene under impact by fullerene projectiles. Materials Today Communications **2022,** 31, 103642.